Superconductor
Science and
Technology

PAPER

Improving critical current density of Nb_3Sn by optimizing pinning potential of grain boundary and grain size

To cite this article: Han-Xi Ren and Cun Xue 2022 *Supercond. Sci. Technol.* **35** 075001

IOP Publishing Superconductor Science and Technology

Supercond. Sci. Technol. **35** (2022) 075001 (11pp) https://doi.org/10.1088/1361-6668/ac6b5f

Improving critical current density of Nb_3Sn by optimizing pinning potential of grain boundary and grain size

Han-Xi Ren and Cun Xue*

School of Mechanics, Civil Engineering and Architecture, Northwestern Polytechnical University,
Xi'an 710072, People's Republic of China

E-mail: xuecun@nwpu.edu.cn

Received 19 February 2022, revised 24 April 2022
Accepted for publication 28 April 2022
Published 13 May 2022

Abstract

Nb_3Sn superconductor is of significant interest for applications in constructing high-field magnets beyond the limit of NbTi. However, its critical current density decreases rapidly at high magnetic fields (>12 T) and the state-of-the-art level of Nb_3Sn superconductors still cannot meet the requirements of the planned future accelerator magnets. The primary flux pinning centers for Nb_3Sn wire mainly arise from the grain boundaries (GBs). In the present paper, we theoretically investigate, through time-dependent Ginzburg-Landau theory and with graphics-processing unit parallel technique, the vortex pinning and the critical current density in large-scale polycrystalline Nb_3Sn superconductor by varying the pinning potential of GB and grain size at various magnetic fields. Unlike the conventional dot-like pinning systems, it is found that the critical current is not a monotonous function by suppressing the superconductivity of the GBs. The optimal pinning potential of GB for maximum critical current density strongly depends on magnetic fields. Furthermore, we find that the critical current density can be significantly enhanced by reducing grain size at low magnetic fields, while increase of critical current density cannot always be observed at high magnetic fields. Actually, critical current density even decreases by reducing grain size, which depends on the superconductivity of GBs. The findings in the paper provide theoretical foundations to achieve further improvement of Nb_3Sn with optimizing the flux pinning.

Supplementary material for this article is available online

Keywords: polycrystalline Nb_3Sn superconductor, vortex pinning, vortex dynamics, critical current density, grain boundary, grain size

(Some figures may appear in colour only in the online journal)

1. Introduction

It is well-known that the practical applications of superconductors are governed by the current-carrying capability without resistance, i.e. critical current density J_c, especially at high magnetic fields. In recent years, the pursuit of high-field magnets beyond the limit of NbTi has expanded dramatically the massive use of Nb_3Sn. With upper critical field around 30 T, critical temperature up to 18.3 K, and high critical current density at high fields (e.g. whole-wire J_c of 1000 Amm^{-2} at 4.2 K, 15 T [1]), Nb_3Sn superconductors have been widely used in dipole and quadrupole magnets for particle accelerators, magnet system for a new generation Electron Cyclotron Resonance ion source (45 GHz) [2, 3], central solenoids and toroidal field coils tokamak fusion devices [4],

---

[*] Author to whom any correspondence should be addressed.

magnetic resonance imaging system [5], nuclear magnetic resonance. Besides the magnetic applications, Nb_3Sn is also used in superconducting radio frequency cavities (for example, Nb_3Sn-Insulator-Nb multilayer structures [6–9]).

For all type-II superconductors, the magnetic flux penetrates into samples in form of quantized magnetic vortices when the external magnetic field exceed the lower critical magnetic field H_{c1}. One needs not pay much attention to the Meissner state as H_{c1} is usually quite weak, for example, H_{c1} of Nb_3Sn is 40 mT. Therefore, the behaviors of magnetic vortices determine the physical properties of type-II superconductors [10, 11], including the current-carrying capability of superconductors (critical current density J_c). The magnetic vortices have non-superconducting cores, which carry the magnetic field lines, surrounded by superconducting currents. When a current flows in a pinning-free superconductor, the vortices will move easily due to the Lorentz force, which dissipates energy and produces a non-zero resistance. So, the vortex motion has a large impact because it leads to increasement of temperature and even causes terrible quench of superconducting devices. Fortunately, the magnetic vortices interacts with non-superconducting defects and can be fixed at these pinning centers in the materials. In this case, the critical current density for practical superconductors is determined by the pinning force to the magnetic vortices in the presence of pinning landscape, which is normally less than depair current density. As a consequence, it is crucial to understand the pinning/depinning behaviors of magnetic vortices because they control the flow of current through the superconductor.

In order to explore the interactions between magnetic vortices and the pinning landscape, various kinds of artificial pinning centers were introduced in superconductors with e-beam nano-lithography in the past decades, such as magnetic dots and holes (antidots) with periodic homonomous and inhomogeneous arrays [12–19]. However, the pinning effect on the magnetic vortices in Nb_3Sn wire mainly arises from the suppressed superconductivity on instinctive grain boundary (GB). It is a very effective approach to improve the critical current density of Nb_3Sn by reducing the grain size [20, 21]. Although the lower treatment temperatures can reduce the grain size and improve the flux pinning, it is also detrimental to the upper critical magnetic field H_{c2} due to the Nb_3Sn phase stoichiometry [22]. On the other hand, the future accelerator magnets need high J_c of Nb_3Sn for bending particle beams. For example, planned future circular collider (FCC) requires J_c with around 2000 Amm^{-2} at 4.2 K, 15 T [23]). However, the state-of-the-art level of Nb_3Sn conductors can reach 1600–1700 Amm^{-2} [24]. Therefore, it is highly needed to improve J_c of Nb_3Sn. In recent years, Xu *et al* found that the Nb_3Sn grain size can be refined by sufficiently supplying oxygen to internally oxidize the Zr in the Nb-1Zr alloy via SnO_2 powder [25–27]. The peak of the pinning force was shifted to 0.3 H_{irr} (the irreversibility field). Despite significant efforts have been made in experiments before, more efforts should be made to further improve flux pinning and J_c in Nb_3Sn conductors in order to meet the requirement of FCC.

Besides the experiments, many researchers theoretically investigate the effects of GB on critical current density [28–34]. Very narrow superconducting-normal-superconducting junctions was used as building blocks for describing GBs in polycrystalline superconductors [35, 36]. Later, for a system with small size, it was found that the critical current density is not sensitive to grain size until the grain size is sufficiently small in polycrystalline superconductors [37], which is not consistent with experiments of Nb_3Sn. It was also found that GBs not only acts as the pinning centers for vortices, but also provides an easy-flow channel for vortex motion [38, 39], which depends on the GB angle [40–42]. However, the previous theoretical works mainly focus on one GB or very small amount of GBs. In order to mimic the realistic polycrystalline Nb_3Sn and optimize J_c by GBs, it is still highly needed to study the vortex pinning and vortex motion in a large number of GBs at present.

In the present paper, employing numerical simulation on graphics-processing units (GPUs), we would like to reveal the vortex statics and dynamics in large-scale polycrystalline Nb_3Sn by time-dependent Ginzburg-Landau (TDGL) theory. The optimization of the critical current density by varying the pinning potential of GBs and grain size is investigated at low and high external magnetic fields. We find variations of J_c with grain size strongly depends on the suppressed superconductivity of GBs at high magnetic field. The paper is organized as follows. The TDGL theory and numerical model are introduced in section 2. Then, in section 3, we discuss the critical current density by varying the pinning potential of GB and grain size, respectively. The summary is given in the last section.

2. Theoretical formalism for vortex pinning by GBs

For superconducting Nb_3Sn wires, as mentioned before, GB is the crucial ingredient to prevent vortex motion. So, as shown in figures 1(a) and (b), we consider a model system of a thin Nb_3Sn film with GBs. In order to gain insight into the critical current density in Nb_3Sn, we calculate the statics and dynamics of superconducting vortices in the pinning landscapes consisting of GBs by using the Ginzburg-Landau theory. Additionally, the conventional dot-like pinning potential is also considered for comparison (see figure 1(c)).

It is well-known that the TDGL equations are based on the Landau's phenomenological theory of second-order phase transitions, which describes the time-evolution and spatial variation of the complex order parameter in superconductors in the presence of a magnetic vector potential [43–47]. Although its formally validity can be only reestablished from the microscopic BCS theory in the vicinity of critical temperature [48], actually it had been found that the TDGL theory is surprisingly accurate (within only a few percent) even at very low temperature by comparing with Eilenberger theory which is valid at all temperatures [49, 50]. So much wider ranges of parameters can be considered, at least qualitatively, or even quantitatively if modified temperature dependencies of relevant quantities are explicitly adopted [43, 51, 52]. In addition to the vortex statics, the TDGL equations can also be used to study slowly vortex configurations [53]. In the past decades, TDGL simulations have been used to reproduce

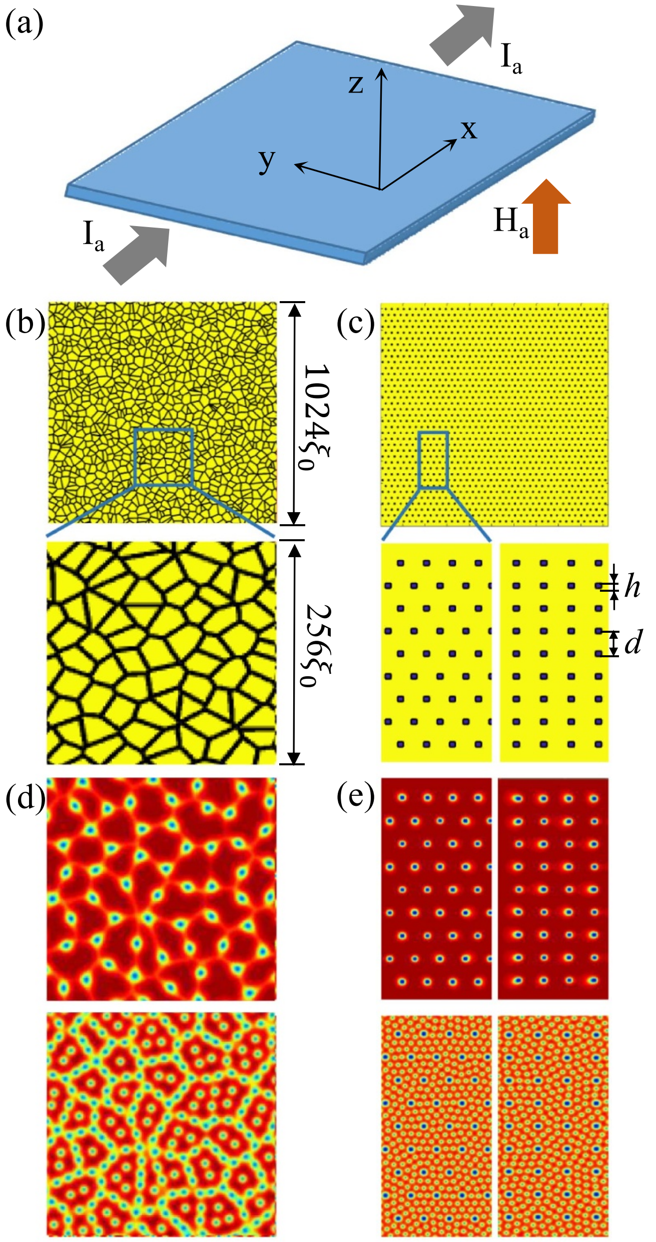

Figure 1. Schematic diagram of numerical models and two different kinds of pinning landscapes (a)–(c) and the simulated vortex states at low and high applied magnetic fields (d) and (e). GBs with tunable grain size and triangular and square periodic arrays of dot-like pinning centers with size of h and period of d. The pinning potential can be tuned by suppressing superconductivity at the pinning centers and GBs by decreasing the Cooper pair density.

and reveal numerous experimental results [54–61]. Therefore, TDGL equations provide an elegant and powerful tool to investigate the vortex statics and dynamics as well as the critical current density, which is far simpler than any microscopic theories.

Using the Landau gauge, $\nabla\cdot\mathbf{A}=0$, TDGL equations can be written in the dimensionless form,

$$u(\partial_t+i\mu)\psi=(\nabla-i\mathbf{A})^2\psi+\epsilon(\mathbf{r})\psi-|\psi|^2\psi+\zeta(\mathbf{r},t) \quad (1)$$

$$\kappa^2\nabla\times(\nabla\times\mathbf{A})=\mathbf{J}_N+\mathbf{J}_S \quad (2)$$

where u is a phenomenological constant that can be derived from the microscopic theory. In the equations, the distances are scaled by the coherence length ξ at the working temperature T_0, the order parameter ψ by its equilibrium value in the absence of magnetic field, the time by the relaxation time $\tau_0=\mu_0\kappa^2\xi_s^2/m_s$, the magnetic field by the upper critical field $H_{c2}=\Phi_0/2\pi\xi^2$, the vector potential by $H_{c2}\xi$, the current density by $J_D=2B_{c2}/3\sqrt{3}\mu_0\xi_s\kappa^2$. By using the following gauge transformation [53],

$$\mu(\mathbf{r})=-xE_x+\tilde{\mu}(\mathbf{r}) \quad (3)$$

$$\psi(\mathbf{r})=\tilde{\psi}(\mathbf{r})e^{iKx} \quad (4)$$

where $\tilde{\mu}$ is a periodic function, and $\tilde{\psi}$ is a quasi-periodic function. K does not depend on $\mathbf{r}$, which satisfies $\partial_t K=E_x$. For Nb$_3$Sn thin film, the penetration length is much larger than the coherence length. So, for the case of high-κ, the magnetic field is nearly homogenous over the sample. We assume the magnetic field H_a is perpendicular to the film, and the vector potential is given by

$$A_x=-H_a y, A_y=0. \quad (5)$$

In order to rule out the edge effect of the sample on the critical current density (edge barrier), the periodic boundary conditions are used along both $x-$ and $y-$axes in our numerical simulations. Under these circumstance, the solutions of the vortex configurations in the presence of complex pinning landscapes can be obtained by solving the following equations,

$$u(\partial_t+i\tilde{\mu})\tilde{\psi}=(\nabla-i\tilde{\mathbf{A}})^2\tilde{\psi}+\epsilon(\mathbf{r})\tilde{\psi}-|\tilde{\psi}|^2\tilde{\psi} \quad (6)$$

$$\Delta\tilde{\mu}=\nabla\,\mathrm{Im}\left[\tilde{\psi}^*(\nabla-i\mathbf{A})\tilde{\psi}\right] \quad (7)$$

$$\partial_t K-\langle\partial_t A_x\rangle+J_{av}-J_{x,ext}=0 \quad (8)$$

where J_{av} is the averaged supercurrent density over the whole simulated region, and $J_{x,ext}$ is the external current applied to the superconducting film along x-axis.

In order to capture the main features of the GBs, the patterns of crystalline grain and GBs are generated by the voronoi diagram randomly. The patterns of crystalline grain are characterized by a tunable averaged grain size. For a fixed averaged grain size, the statistics of grain size satisfy Gaussian distribution, which will be discussed in detail later. The pinning effects can be induced by suppressing the superconductivity of the GBs in numerical simulations, which can be tuned via the function $\varepsilon(\mathbf{r})$ in the TDGL equations. In addition, the simulated region should be sufficiently large to eliminate the disturbance of critical current density induced by the randomly generated GBs with voronoi diagram. Therefore, we use the large-scale computational algorithm for TDGL equations proposed by Sadovskyy *et al* with massively parallel architectures implemented on a GPU (see details in [53]). As shown in figure 1(b), the simulated region with 1024×1024 (2048×2048 grids) is suitable to ensure that the deviation of critical current density for different randomly generated GB is less than 1% (see more details in appendix A). The grid size is 0.6 in all numerical simulations because we find it is suitable after checking the simulated results by varying grid size within 0.5–0.7. We implement the numerical simulations on an NVIDIA GPU with single precision (GeForce RTX 3080/3090 with 10/24 GB of memory powered by Ampere architecture) using the compute unified device architecture (CUDA). Details for the CUDA programming model with GPU architecture can be seen in [51, 62]. The critical current density are obtained from the current–voltage (I–V) characteristics with a threshold value 10^{-4}.

3. Results and discussions

In a first step, we briefly discuss the static vortex states in the presence of GBs and the conventional periodic arrays of dot-like artificial pinning centers (square and triangular arrays). In order to clearly show vortex states, we only present partial region rather than whole simulated region in all figures. As shown in figures 1(d) and (e), all the vortices are pinned by the dot-like pinning centers at low applied magnetic field. Similarly, all vortices are pinned by GBs and the vortices prefer staying at the intersections of the GBs. At high magnetic field, besides the pinned vortices, the interstitial vortices can be observed in the sample. It was reported that the interstitial vortices are highly mobile under applied current, which leads to a strong reduction of the critical current of the system. In the following section, we will unveil the different characteristics of flux pinning and flux motion in such two pinning systems. Unless otherwise stated, all physical variables are dimensionless in the following text.

3.1. *Critical current density by optimizing pinning potential of GB*

As shown in figure 2, the critical current density keeps increasing when the Cooper pair density of the dot-like pinning centers ($|\widetilde{\psi}|_{dot}$) is decreased. This indicates that the pinning effect on the vortices becomes stronger by reducing the superconductivity at the pinning centers, which can enhance the critical current density. As a consequence, maximum critical current density can be obtained when the superconductivity of dot-like pinning centers is completely suppressed (e.g. holes) because of the monotonic variations of J_c with $|\widetilde{\psi}|_{dot}$. For the dot-like pinning systems, the pinning centers are separated. In this case, as shown in panels 1–2, the vortices must be first driven out from the pinning dots before continuous vortex motion.

Unlike the dot-like pinning systems, the GBs connect each other, thereby forming a net-like pattern in the plane. In this subsection, the averaged grain size is fixed with 40 in numerical simulations. The coherence length of pure Nb_3Sn is about 3 nm [63]. So the averaged grain size is about 120 nm in SI unit. The thickness of GBs used in all TDGL simulations is 0.6ξ–1.2ξ, which is about 1.8–3.6 nm. Experiments by atom probe tomography show that the averaged GB thickness in realistic Nb_3Sn wires is approximately 2 nm [64, 65]. So the GB thickness used in the TDGL simulations is very close to the realistic case.

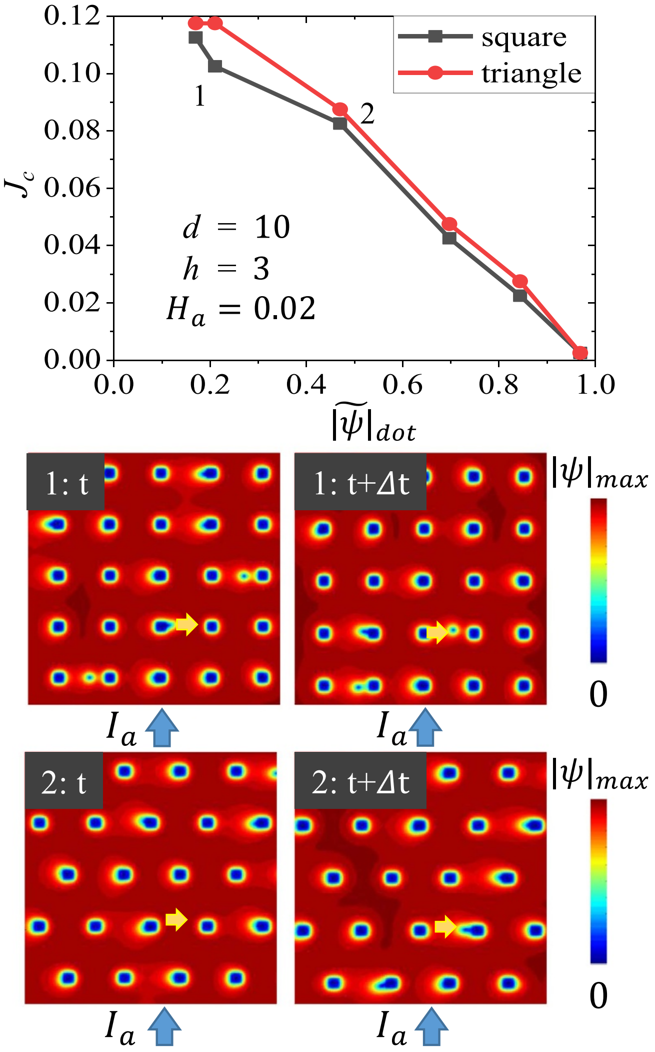

Figure 2. Variations of the critical current density with the Cooper pair density in the square and triangular periodic arrays of dot-like pinning centers obtained at applied magnetic field $H_a = 0.02$. The size and period of pinning dots are $h = 3$ and $d = 10$ ($h \approx 9$ nm and $d \approx 30$ nm in SI units), respectively. The panels of the Cooper pair density show the snapshots of the vortex motions through the square and triangular pinning array obtained at two close time when the applied current is slightly more than critical current. The cooper pair density of dot-like pinning centers is indicated on the J_c curves.

Figure 3 shows the variations of simulated voltage with increasing applied current. At low magnetic field, one can find that the voltage increases smoothly when the applied current exceeds J_c. In order to gain insight the vortex motion in this stage, panel 1 show the snapshots of Cooper pair density at two close time under low magnetic field ($H_a = 0.005$) that is indicated on I–V curves. There are not interstitial vortices and vortices move along the GBs. In this case, the Lorentz force is not sufficiently large to drag the vortices out of the GBs. When the applied current is sufficiently large, as shown in panel 2,

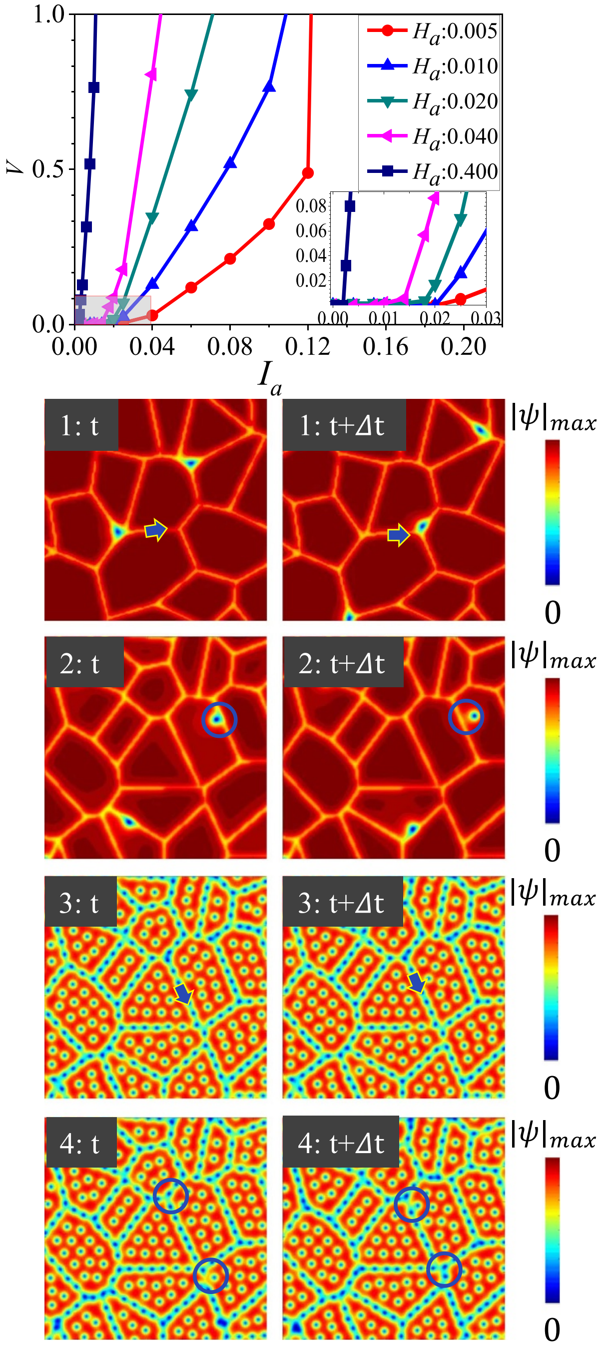

Figure 3. Current–voltage (I–V) characteristics in the superconducting film with GB at different applied magnetic fields. The averaged Cooper pair density at GB $|\widetilde{\psi}|_{GB} = 0.73$. Panels 1–4 of Cooper pair density shows the snapshots of slow and fast vortex motions through the GBs with applied current indicated on the I–V curves at low and high applied magnetic filed ($H_a = 0.005$ and 0.4). The blue arrows show the directions of vortex motion and the blue circles shows the vortices move across the GBs. The vortex motion can be seen in supplementary movies.

one can observe that the vortices can move from one crystalline grain to another one across the GBs and velocity of the moving vortices is quite fast, which lead to a voltage jumps in the I–V curves (see point 2 on I–V curves). The similar results were also observed in other systems, such as dynamic pinning potential [66, 67] and slit array of pinning sites [68]. At higher magnetic fields, the vortices move slowly along the GBs but the interstitial vortices does not move out when the applied current is slightly larger than critical current density (see panel 3). With increasing current, panel 4 shows that all vortices move fast, which lead to a high voltage. The vortex motions for panels 1–4 can been seen in supplementary movies (available online at stacks.iop.org/SUST/35/075001/mmedia). Therefore, unlike the dot-like pinning systems, the interconnected GBs not only provide pinning effect on the vortices, but also provide easy-flow channels for vortices (especially the GBs parallel to the Lorentz force).

The pinning effect of the GBs is mainly attributed to their suppressed superconductivity. So, we start to explore the critical current density by varying the Cooper pair density at GBs and the GB pattern is fixed. Although it is usually difficult to control the Cooper pair density of GBs during the real manufacture process of Nb_3Sn wire, GB characteristics may be adjusted by some possible methods. The normal precipitation like Cu or Ti may have effect on the superconductivity of GB [65] and the segregation of Cu and Ti had been detected in almost all GBs [64, 69]. Another possible method may be hot pressing to improve the GB property, which had been successfully used in iron based superconducting wires [70, 71]. In experiments, the low-temperature scanning tunneling spectroscopy (STS) provides an elegant tool to detect the superconducting condensate with atomic resolution [72]. With STS technique, it was reported that twin boundaries noticeably suppress the superconducting gap in iron-based superconductors [73]. So, it may be possible to use STS to measure the superconducting gap at GBs and other regions. One may link the suppressed Cooper pair density at GBs with the difference between superconducting gap at GBs and far away from GBs, which would provide important information for the optimizing the pinning effect of GBs.

Figure 4 shows the critical current density as a function of applied magnetic field obtained at different Cooper pair density of the GBs. One can find that the critical current density in superconducting film with GBs is nearly an exponential function of applied magnetic field. However, for the samples with GBs at weak magnetic field $H_a < 0.05$ or samples without GBs, the critical current density decreases even faster than exponential function. Moreover, it is interesting that the critical current density first increases and then decreases by suppressing the Cooper pair density of GBs, which is different from the dot-like pinning system. In this case, maximum critical current density should be observed by varying the Cooper pair density of GBs. Panels 1–6 show the static vortex states in GBs with different suppressing superconductivity at low and high magnetic fields (indicated on the $J_c(H_a)$ curves). Panels 1 and 4 demonstrate that the vortices are not circular pearl vortices at the GBs with small $|\widetilde{\psi}|_{GB}$. In this case, the vortices can move quite easily and small applied current can lead to flux flow along the GBs. The validation of TDGL simulations for J_c with GBs by the scaling law from experiments can be seen in appendix B.

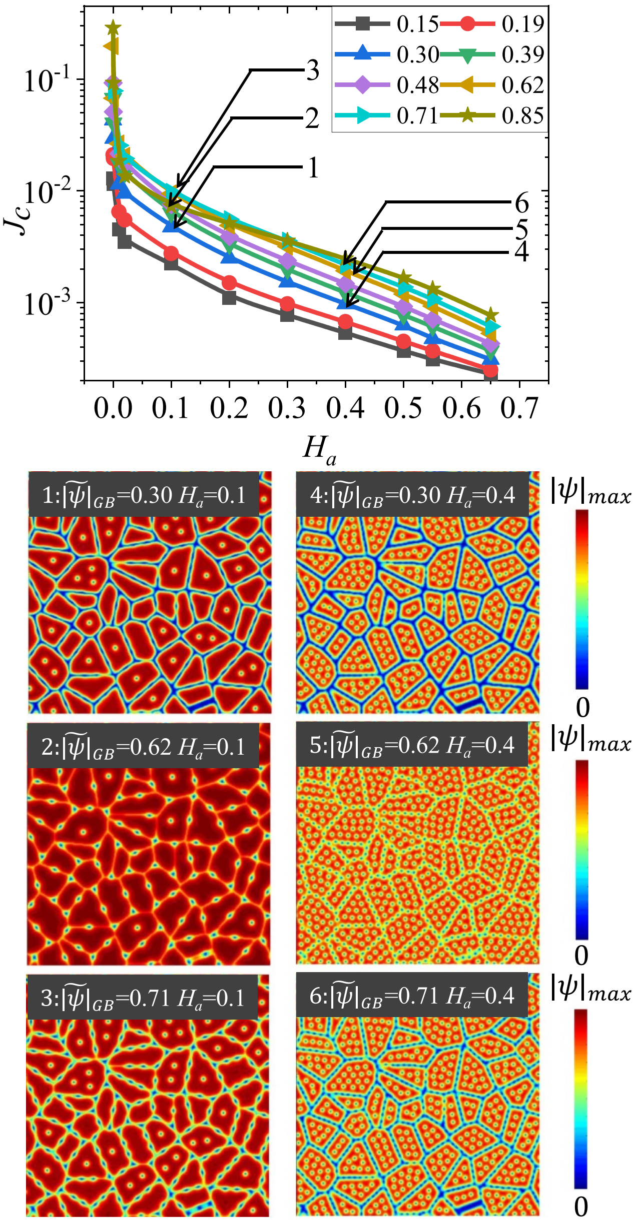

Figure 4. Simulated critical current density J_c as a function of applied magnetic field H_a obtained for different $\widetilde{|\psi|}_{GB}$. Panels 1–6 represent the simulated Cooper pair density of static vortex states obtained at $H_a = 0.1$ and 0.4.

In order to obtain the maximum critical current density, we further explore the optimal Cooper pair density of GBs. As shown in figure 5(a), the critical current is indeed not a monotonic function of $\widetilde{|\psi|}_{GB}$. By suppressing the superconductivity of GBs, one can find that the critical current density increases to a peak value and then decreases. Therefore, the maximum critical current density can be obtained by varying the Cooper pair density of the GBs. Additionally, the optimal Cooper pair density for maximum critical current density depends on applied magnetic field, which is shown in figure 5(b). It can be found that the suppression of superconductivity at GBs should be decreased with applied magnetic field. In particular, at high magnetic field $H_a > 0.4$ (>11 T for Nb_3Sn in SI unit), the optimal Cooper pair density should be more than 0.85 in order to obtain the high critical current density. In the absence of applied current, panels 1–4 show the static vortex states for the best Cooper pair density of GBs at different magnetic fields that are indicated on the curve of figure 5(b).

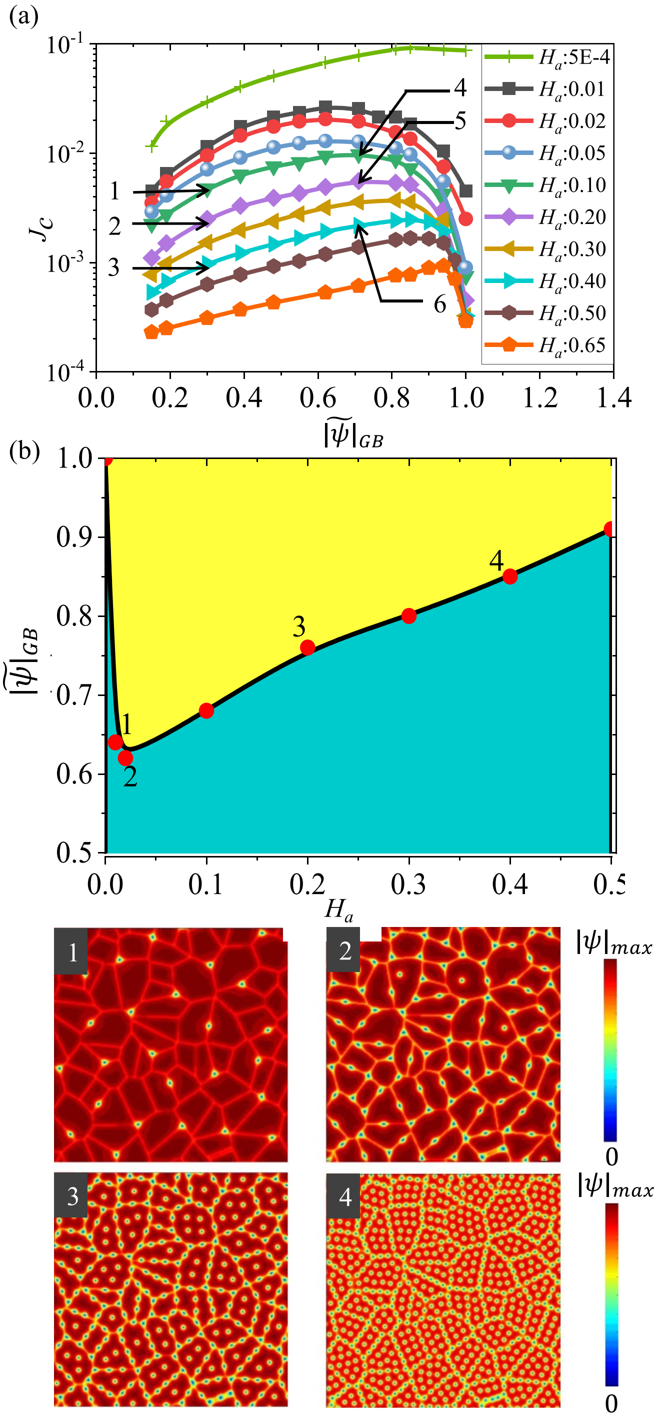

Figure 5. Variations of critical current density J_c with $\widetilde{|\psi|}_{GB}$ obtained at different magnetic fields (a). The optimal $\widetilde{|\psi|}_{GB}$ as a function of applied magnetic field H_a in order to obtain maximum critical current density (b). Panels 1–4 show the simulated static vortex states obtained at different magnetic fields with optimal $\widetilde{|\psi|}_{GB}$.

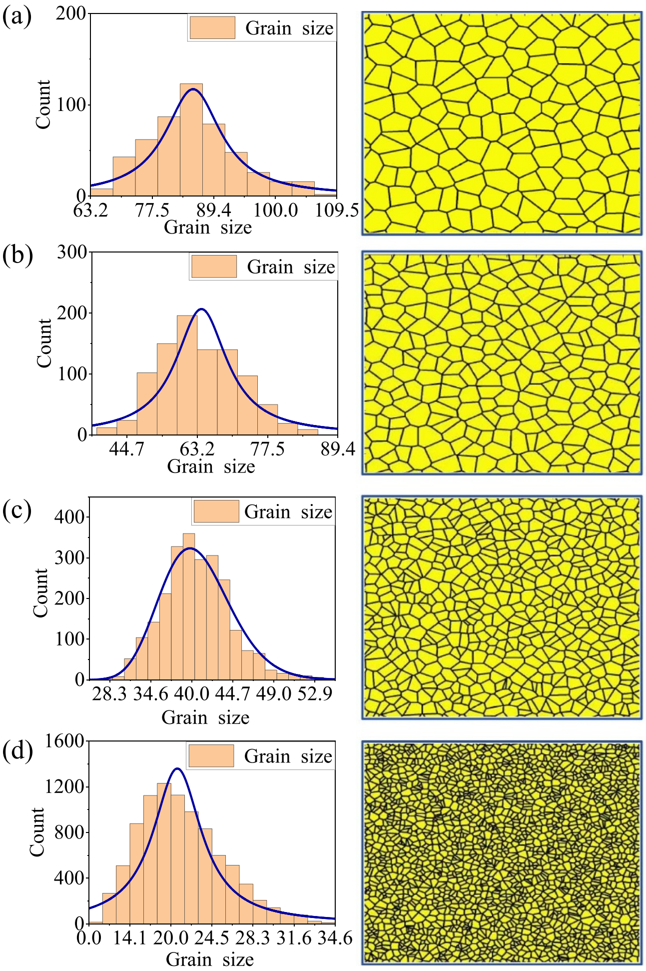

Figure 6. Histogram of crystalline grain size in generated GB patterns with different averaged grain size. The right panels show the whole patterns of GBs generated by voronoi method, which is used to calculate the critical current density in TDGL simulations.

3.2. *Critical current density by varying grain size*

Besides the Copper pair density of GBs, experiments demonstrate that the critical current density of Nb_3Sn can be enhanced by refining the grain [25, 27]. In this subsection, patterns of crystalline grains with tunable averaged grain size are generated by voronoi method, which are used to calculated the critical current density by TDGL simulations. The histogram of grain size in figure 6 show that the crystalline grains almost satisfy a Gaussian distribution (blue curves), which indicates that the patterns of crystalline grains are reasonable to mimic the real morphology of Nb_3Sn. Additionally, the number of crystalline grains is sufficiently large in the simulated region to avoid the disturbance of different patterns of GBs generated randomly. This can be verified by the fact that the critical current density are nearly the same for generating different patterns of GBs with fixed averaged grain size.

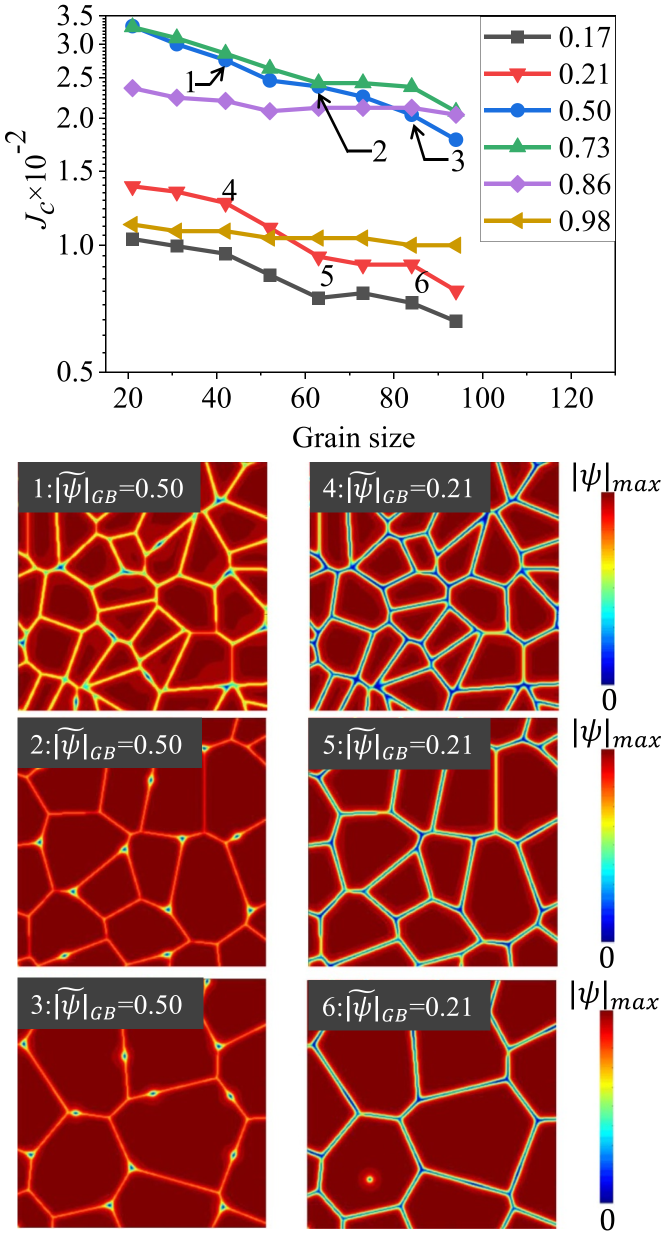

Figure 7. Simulated critical current density J_c as a function of grain size for different $|\widetilde{\psi}|_{GB}$ obtained at low magnetic field ($H_a = 0.005$). Panels 1–6 show the simulated vortex states with grain size and $|\widetilde{\psi}|_{GB}$ indicated on the J_c curves.

As shown in figure 7, at low applied magnetic field, the critical current density decreases as the grain size is increased. This is consistent with experimental results of Nb_3Sn superconducting wires. One may suppose that the decrease of critical current density should be attributed to the appearance of more interstitial vortices with increasing the grain size. However, this is not exact. Panels 1–3 (4–6) show the vortex states with different grain size for $|\widetilde{\psi}|_{GB} = 0.5$ (0.21). Actually, the interstitial vortices are not observed even in large grain size for $|\widetilde{\psi}|_{GB} = 0.5$ due to the quite small applied magnetic field. Furthermore, for $|\widetilde{\psi}|_{GB} = 0.21$, there are seldom interstitial vortices observed when grain size is more than 80. But this does not lead to a rapid decrease of J_c. Therefore, our numerical simulations show that the interstitial vortices do not have such significant impact on critical current density as it is supposed. The disordered orientations of GBs, especially the increase of GB with large angles to the vortex motion, should also be responsible for enhancing J_c as the grain size is decreased. As

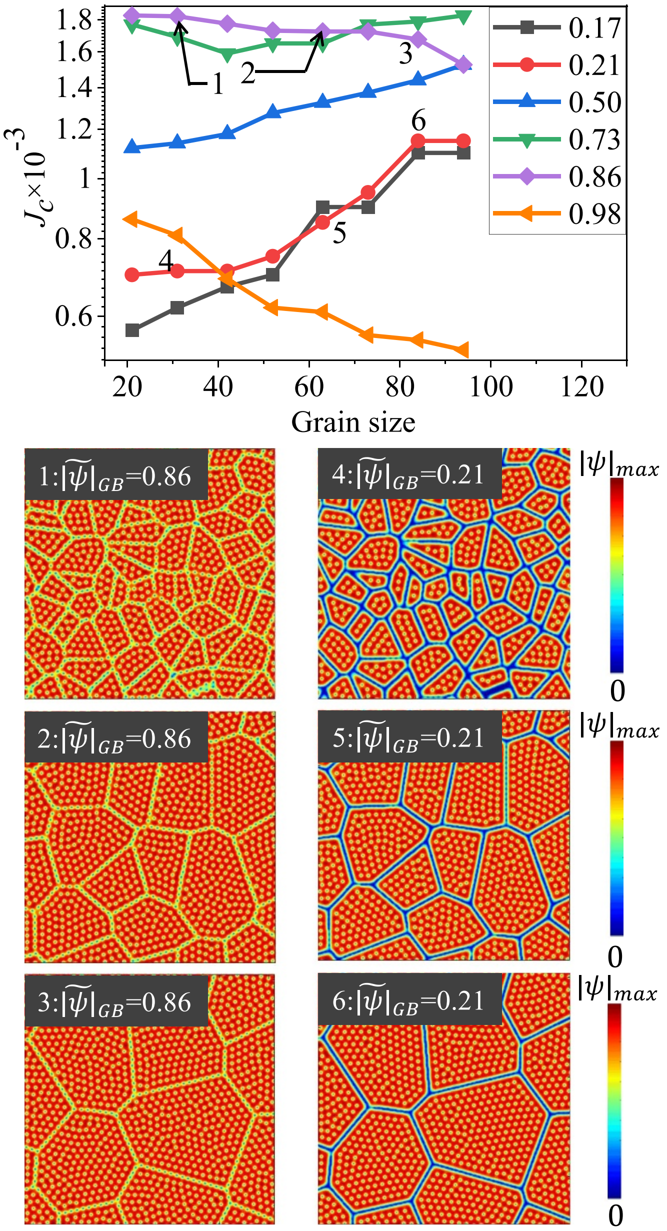

Figure 8. Variations of simulated critical current density with grain size at high magnetic field $H_a = 0.5$ and the simulated vortex states (panels 1–6) at points indicated on the curves. Other parameters are the same with those in figure 7. The vortex motion for panels 1, 2, 4, and 5 can be seen in supplementary movies.

shown in figure 7, the simulated results further demonstrate that the decreasing rate of J_c with grain size also depends on the suppressed superconductivity of GB.

Finally, we discuss the variation of critical current density with grain size at high applied magnetic field $H_a = 0.5$. As shown in figure 8, the critical current density decreases slightly by increasing the grain size if the superconductivity of GB is suppressed slightly. However, the critical current density can be enhanced with increasing the grain size when the averaged Cooper pair density $|\widetilde{\psi}|_{GB}$ <0.73, which is contrary to the case of large $|\widetilde{\psi}|_{GB}$. In order to understand the reversal variations of the critical current density with grain size, as shown in panels 1–6, we calculate the vortex states for different grain sizes obtained at $|\widetilde{\psi}|_{GB} = 0.86$ (panels 1–3) and 0.21 (panels 4–6), respectively. It can be found that the pinning effect of GBs dominates at $|\widetilde{\psi}|_{GB} = 0.86$. In this case, the critical current density can be enhanced by increasing the GBs. However, at $|\widetilde{\psi}|_{GB} = 0.21$, the superconductivity of GBs is strongly suppressed and the vortices moves more easily along GBs. Therefore, the critical current density decreases due to the more easy-flow channels by refining grain sizes.

4. Summary

With higher upper magnetic field and critical current density, Nb_3Sn superconducting wires are more preferable to construct high-field magnets (beyond the limit of NbTi, > 10 T) than the costly and not-yet-mature high temperature superconductors (for example, difficult quench protection). Nevertheless, the planed future accelerator magnets requires Nb_3Sn superconductors with even more excellent performance, especially in critical current density. To mimic the pinning centers in polycrystalline polycrystalline Nb_3Sn, large-scaled pinning landscape consisting of GBs is generated and we theoretically investigate the flux pinning in Nb_3Sn superconductor with TDGL theory, including the vortex statics and dynamics in the presence of GBs. Furthermore, in order to further improve the critical current density by optimizing flux pinning, we calculate and discuss the critical current density of polycrystalline Nb_3Sn by varying the pinning potential of GBs and grain size at various magnetic fields.

(a) The critical current density does not always increase by suppressed the Cooper pair density of the GBs, which is significantly different from the dot-like pinning systems. When the superconductivity of GBs are suppressed too much, the magnetic flux move easily along the GBs, thereby forming easy flux channels. The optimal pinning potential of GBs for maximum critical current density strongly depends on the magnetic fields. In order to obtain high critical current density at high magnetic fields ($0.3 < H_a < 0.5$), the desired interval of Cooper pair density at GBs should be between 0.8 and 0.9.

(b) The critical current density can be enhanced by refining the grain size at low magnetic fields. However, the variations of critical current density is quite complex at high magnetic fields. For example, with reducing the grain size at $H_a = 0.5$, the critical current density only increases when the superconductivity of GBs is slightly suppressed, while it even decreases for Cooper pair density of GBs is less than 0.73. Therefore, besides the grain size, the pinning potential of GBs should also be considered to improve the critical current density, especially at high external magnetic fields.

Data availability statement

The data that support the findings of this study are available upon reasonable request from the authors.

Acknowledgment

We acknowledge support by the National Natural Science Foundation of China (Grant Nos. 11972298 and 12011530143).

Appendix A. J_c of randomly generated GBs

Besides the GB pattern used in main text, as shown in figure 9, we also create other two random GB patterns (GB 2 and GB 3) by the voronoi diagram. These different GB patterns have a fixed averaged grain size 38 (about 115 nm in SI unit). We calculate the critical current density for the three different GB patterns with two different averaged Cooper pair density, i.e. $|\widetilde{\psi}|_{GB} = 0.73$ and 0.21, respectively. The simulated results show that the critical current density are almost the same. This indicates that the simulated region is sufficiently large and the simulated critical current density is a statistical result, which is independent on the randomly created GB patterns.

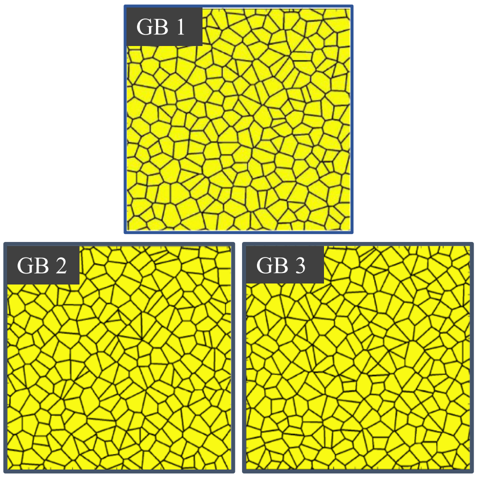

Figure 9. Three different GB patterns with a fixed grain size 38 (about 115 nm in SI unit) generated by voronoi diagram. The simulated critical current density J_c are 0.0243 (GB 1), 0.0246 (GB 2), 0.0242 (GB 3) for $|\widetilde{\psi}|_{GB} = 0.73$, respectively. J_c are 0.0094 (GB 1), 0.0093 (GB 2), 0.0094 (GB 3) for $|\widetilde{\psi}|_{GB} = 0.21$, respectively.

Appendix B. Validation of TDGL simulations for J_c with GBs

In order to verify the TDGL simulations for J_c of polycrystalline Nb_3Sn superconductor with GBs, here we check the variations of critical current density J_c with applied magnetic field H_a obtained by TDGL simulations (see figure 4). Due to the magnitude of J_c of Nb_3Sn wires depends on the manufacture techniques, instead of comparing with specific experimental value of J_c, we compare the simulated results with the well-known scaling law [74] and one modified scaling law [75] that had been confirmed by many experiments [76]. As shown in figure 10, one can see our simulations are in consistent with both scaling law and modified scaling law quite well.

For polycrystalline materials with GBs, for example, Nb_3Sn and Nb_3Al, experimental measurements demonstrate that the dependence of J_c on magnetic field can be described by the Kramer scaling law approximately [77, 78]. The Kramer scaling law mainly reflects the influence of GBs on the flux vortex and critical current through flux-shear models. Later, modified scaling law was proposed, which is valid for more superconductors. It was reported that the modified scaling law even agrees well with experiments in the case of polycrystalline superconductors with artificial pinning centers (APC) [79].

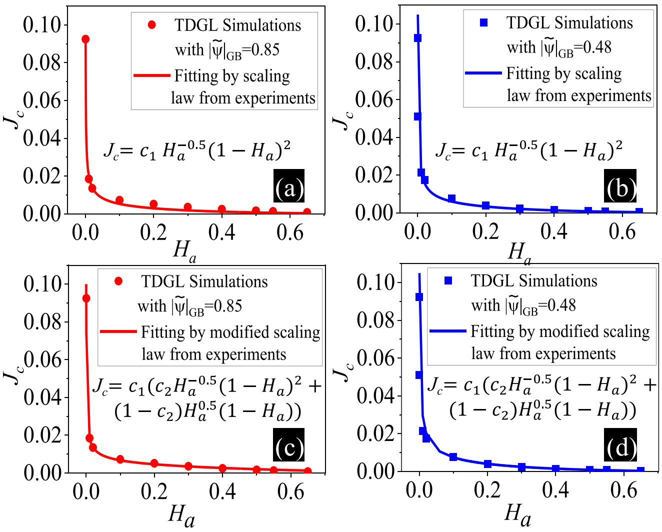

Figure 10. The critical current density obtained by TDGL simulations for $|\widetilde{\psi}|_{GB} = 0.85$ and 0.48. The fitting curves are the well-known scaling law [74] (a) and (b) and modified scaling law [75] (c) and (d) that had been confirmed by many experiments [76].

ORCID iD

Cun Xue https://orcid.org/0000-0001-6255-2837

References

[1] Ghosh A K, Cooley L D, Moodenbaugh A R, Parrell J, Field M B, Zhang Y and Hong S 2005 *IEEE Trans. Appl. Supercond.* **15** 3494
[2] Sun L *et al* 2020 *Rev. Sci. Instrum.* **91** 023310
[3] Wang Q Y, Xue C, Chen Y Q, Ou X J, Wu W, Liu W, Ma P, Sun L T, Zhao H W, Zhou Y H 2021 *Physica* C **593** 1354002
[4] For The Press, Facts And Figures 2021 (available at: http://iter.org/factsfigures/)
[5] Baig T, Yao Z, Doll D, Tomsic M and Martens M 2014 *Supercond. Sci. Technol.* **27** 125012
[6] Gurevich A 2017 *Supercond. Sci. Technol.* **30** 034004
[7] Kubo T 2017 *Supercond. Sci. Technol.* **30** 094004
[8] Posen S and Hall D L 2017 *Supercond. Sci. Technol.* **30** 033004
[9] Wang Q-Y, Xue C, Dong C and Zhou Y-H 2022 *Supercond. Sci. Technol.* **35** 045004
[10] Gammel P 2001 *Nature* **411** 434
[11] Wang Y-L, Ma X Y, Xu J, Xiao Z-L, Snezhko A, Divan R, Ocola L E, Pearson J E, Janko B and Kwok W-K 2018 *Nat. Nanotech.* **13** 560
[12] Berdiyorov G R, Milošević M V and Peeters F M 2006 *Phys. Rev. Lett.* **96** 207001
[13] Misko V, Savel'ev S and Nori F 2005 *Phys. Rev. Lett.* **95** 177007
[14] Kramer R B G, Silhanek A V, Van de Vondel J, Raes B and Moshchalkov V V 2009 *Phys. Rev. Lett.* **103** 067007
[15] Silhanek A V, Gillijns W, Moshchalkov V V, Zhu B Y, Moonens J and Leunissen L H A 2006 *Appl. Phys. Lett.* **89** 152507
[16] Milošević M V and Peeters F M 2004 *Phys. Rev. Lett.* **93** 267006
[17] Ray D, Olson Reichhardt C J, Jankó B and Reichhardt C 2013 *Phys. Rev. Lett.* **110** 267001
[18] Wang Y L, Latimer M L, Xiao Z L, Divan R, Ocola L E, Crabtree G W and Kwok W K 2013 *Phys. Rev.* B **87** 220501(R)
[19] Motta M, Colauto F, Ortiz W A, Fritzsche J, Cuppens J, Gillijns W, Moshchalkov V V, Johansen T H, Sanchez A and Silhanek A V 2013 *Appl. Phys. Lett.* **102** 212601
[20] Scanlan R M, Fietz W A and Koch E F 1975 *J. Appl. Phys.* **46** 2244
[21] Schauer W and Schelb W 1981 *IEEE Trans. Magn.* **17** 374
[22] Xu X, Sumption M D and Collings E W 2014 *Supercond. Sci. Technol.* **27** 095009
[23] Parrell J A, Zhang Y, Field M B, Meinesz M, Huang Y, Miao H P, Hong S, Cheggour N and Goodrich L 2009 *IEEE Trans. Appl. Supercond.* **19** 2573
[24] Cooley L D, Ghosh A K, Dietderich D R and Pong I 2017 *IEEE Trans. Appl. Supercond.* **27** 6000505
[25] Xu X, Sumption M D, Peng X and Collings E W 2014 *Appl. Phys. Lett.* **104** 082602
[26] Xu X, Sumption M D and Peng X 2015 *Adv. Mater.* **27** 1346
[27] Xu X 2017 *Supercond. Sci. Technol.* **30** 093001
[28] Carty G J and Hampshire D P 2008 *Phys. Rev.* B **77** 172501
[29] Sunwong P, Higgins J S, Tsui Y, Raine M J and Hampshire D P 2013 *Supercond. Sci. Technol.* **26** 095006
[30] Reichhardt C, Olson C and Nori F 2000 *Phys. Rev.* B **61** 3665
[31] Xue F, Gu Y and Gou X 2016 *J. Supercond. Novel Magn.* **29** 2711
[32] Asai H and Watanabe S 2008 *Phys. Rev.* B **77** 224514
[33] Xue F, Gu Y and Gou X 2016 *J. Supercond. Novel Magn.* **29** 2711
[34] Hilgenkamp H and Mannhart J 2002 *Rev. Mod. Phys.* **74** 485
[35] Carty G J and Hampshire D P 2013 *Supercond. Sci. Technol.* **26** 065007
[36] Blair A I and Hampshire D P 2018 *IEEE Trans. Appl. Supercond.* **28** 8000205
[37] Blair A I and Hampshire D P 2019 *IEEE Trans. Appl. Supercond.* **29** 8001705
[38] Jiang L, Xu W W, Hua T, Yu M, An D Y, Chen J, Jin B B, Kang L and Wu P H 2015 *Sci. China Technol. Sci.* **58** 493
[39] Duran C A, Gammel P L, Wolfe R, Fratello V J, Bishop D J, Rice J P and Ginsberg D M 1992 *Nature* **357** 474
[40] Liu Y, Gou X-F and Xue F 2021 *Chin. Phys.* B **30** 097402
[41] Vlasko-Vlasov V K, Dorosinskii L A, Polyanskii A A, Nikitenko V I, Welp U, Veal B W and Crabtree G W 1994 *Phys. Rev. Lett.* **72** 3246
[42] Zhu B Y, Dong J, Xing D and Wang Z D 1998 *Phys. Rev.* B **57** 5075
[43] Ginzburg V L 1955 *Zh. Eksp. Teor. Fiz.* **3** 621
[44] Tinkham M 1975 *Introduction to Superconductivity* (New York: McGraw-Hill)
[45] Kato R, Enomoto Y and Maekawa S 1991 *Phys. Rev.* B **44** 6916
[46] Gropp W D, Kaper H G, Leaf G K, Levine D M, Palumbo M and Vinokur V M 1996 *J. Comput. Phys.* **123** 254
[47] Winiecki T and Adams C S 2002 *J. Comput. Phys.* **179** 127
[48] Gor'kov L P 1959 *Sov. Phys. JETP* **9** 1364
[49] Catelani G and Sethna J P 2008 *Phys. Rev.* B **78** 224509
[50] Pack A R, Carlson J, Wadsworth S and Transtrum M K 2020 *Phys. Rev.* B **101** 144504
[51] Stošić D, Stošiá D, Ludermira T, Stošić B and Milošević M V 2016 *J. Comput. Phys.* **322** 183
[52] Müller A, Milošević M V, Dale S E C, Engbarth M A and Bending S J 2012 *Phys. Rev. Lett.* **109** 197003
[53] Sadovskyy I A, Koshelev A E, Phillips C L, Karpeyev D A and Glatza A 2015 *J. Comput. Phys.* **294** 639
[54] Xue C, Ge J Y, He A, Zharinov V S, Moshchalkov V V, Zhou Y H, Silhanek A V and Van de Vondel J 2017 *Phys. Rev.* B **96** 024510
[55] Xue C, Ge J-Y, He A, Zharinov V S, Moshchalkov V V and Zhou Y-H 2018 *New J. Phys.* **20** 093030

[56] Ge J-Y, Gladilin V N, Tempere J, Xue C, Devreese J T, Van de Vondel J, Zhou Y H and Moshchalkov V V 2016 *Nat. Commun.* **7** 13880
[57] Sadovskyy I A, Koshelev A E, Glatz A, Ortalan V, Rupich M W and Leroux M 2016 *Phys. Rev. Appl.* **5** 014011
[58] Berdiyorov G R, Milosevic M V, Latimer M L, Xiao Z L, Kwok W K and Peeters F M 2012 *Phys. Rev. Lett.* **109** 057004
[59] Sadovskyy I A, Koshelev A E, Glatz A, Ortalan V, Rupich M W and Leroux M 2016 *Phys. Rev. Appl.* **5** 014011
[60] Sadovskyy I A *et al* 2016 *Adv. Mater.* **28** 4593
[61] Zhang F, Wang L, Qi B, Zhao B, Ko E E, Riggan N D, Chin K and Qiao H 2017 *Proc. Natl Acad. Sci.* **114** E10274
[62] NVIDIA Corporation, CUDA Toolkit Documentation 2021 (available at: https://docs.nvidia.com/cuda/index.html/)
[63] Suenaga M and Jansen W 1983 *Appl. Phys. Lett.* **43** 791
[64] Sandim M J R, Tytko D, Kostka A, Choi P, Awaji S, Watanabe K and Raabe D 2013 *Supercond. Sci. Technol.* **26** 055008
[65] Banno N, Morita T, Yu Z, Yagai T and Tachikawa K 2019 *Supercond. Sci. Technol.* **32** 115017
[66] Xue C, He A, Milošević M V, Silhanek A V and Zhou Y-H 2019 *New J. Phys.* **21** 113044
[67] He A, Xue C and Zhou Y-H 2019 *Appl. Phys. Lett.* **115** 032602
[68] He A and Xue C 2020 *Chin. Phys.* B **29** 127401
[69] Cantoni M, Abächerli V, Uglietti D, Seeber B and Flükiger R 2008 *Microsc. Microanal.* **14** 1146
[70] Weiss J D, Tarantini C, Jiang J, Kametani F, Polyanskii A A, Larbalestier D C and Hellstrom E E 2012 *Nat. Mater.* **11** 682
[71] Zhang X *et al* 2014 *Appl. Phys. Lett.* **104** 202601
[72] Panghotra R, Timmermans M, Xue C, Raes B, Moshchalkov V V and Van de Vondel J 2019 *Phys. Rev.* B **100** 054519
[73] Song C-L, Wang Y-L, Jiang Y-P, Wang L, He K, Chen X, Hoffman J E, Ma X-C and Xue Q-K 2012 *Phys. Rev. Lett.* **109** 137004
[74] Kramer E J 1973 *J. Appl. Phys.* **44** 1360
[75] Rodrigues D, Da Silva L B S, Rodrigues C A, Oliveira N F and Bormio-Nunes C 2011 *IEEE Trans. Appl. Supercond.* **21** 3150
[76] Xu X, Rochester J, Peng X, Sumption M and Tomsic M 2019 *Supercond. Sci. Technol.* **32** 02LT01
[77] Taylor D M J and Hampshire D P 2005 *Supercond. Sci. Technol.* **18** S241
[78] Keys S A and Hampshire D P 2003 *Supercond. Sci. Technol.* **16** 1097
[79] Baumgartner T, Eisterer M, Weber H W, Flükiger R, Scheuerlein C and Bottura L 2015 *Sci. Rep.* **5** 10236